Condensation formation by impulsive heating in prominences

J. T. Karpen and S. K. Antiochos

E. O. Hulburt Center for Space Research, Naval Research Laboratory, Washington, DC, 20375-5352

judy.karpen@nrl.navy.mil

ABSTRACT

Our thermal nonequilibrium model for prominence formation provides an explanation for the well-observed presence of predominantly dynamic, cool, dense, material suspended in the corona above filament channels. According to this model, condensations form readily along long, low-lying magnetic field lines when heating is localized near the chromosphere. Often this process yields a dynamic cycle in which condensations repetitively form, stream along the field, and ultimately disappear by falling onto the nearest footpoint. Our previous studies employed only steady heating, as is consistent with some coronal observations, but many coronal heating models predict transient episodes of localized energy release (*e.g.,* nanoflares). Here we present the results of a numerical investigation of impulsive heating in a model prominence flux tube and compare the outcome with previous steady-heating simulations. We find that condensations form readily when the average interval between heating events is less than the coronal radiative cooling time ($\sim$2000 s). As the average interval between pulses decreases, the plasma evolution more closely resembles the steady heating case. The heating scale and presence or absence of background heating also determine whether or not condensations form and how they evolve. Our results place important constraints on coronal heating in filament channels, and strengthen the case for thermal nonequilibrium as the process responsible for the plasma structure in prominences.

Subject headings: Sun: prominences — Sun: magnetic fields — Sun: corona

1. Introduction

Recent observations by the Solar and Heliospheric Observatory (SOHO), Transition Region and Coronal Explorer (TRACE), the Swedish Vacuum Solar Telescope (SVST), and

the Very High Angular Resolution Ultraviolet Telescope (VAULT) reveal fine-scale counterstreaming flows and proper motions, and much more spatial and temporal complexity than previously detected (*e.g.,* Lin *et al.* 2003, 2005; Vourlidas & Korendyke 2004). The overwhelming impression left by these detailed observations is that the bulk of the prominence mass is in the form of transient, moving knots and longer horizontal threads that condense *in situ* in the corona.

Our thermal nonequilibrium model for prominence condensations, which we have explored extensively through theoretical analysis and 1D numerical simulations, predicts observable signatures such as the thermal properties, velocity, and mass of moving features in long low-lying flux tubes typical of the core of filament channels. By thermal nonequilibrium we mean the catastrophic and dynamic consequence of an imbalance among the energy sources and sinks in coronal plasmas within flux tubes longer than $\sim$8 times the heating deposition scale (Serio *et al.* 1981; Mok *et al.* 1990; Antiochos & Klimchuk 1991; Dahlburg, Antiochos, & Klimchuk 1998; Antiochos *et al.* 1999). In our investigations of this process, we found that condensations form readily along long, low-lying magnetic field lines when the heating is localized near the chromosphere, as is consistent with several coronal-loop analyses (*e.g.,* Aschwanden, Schrijver, & Alexander 2001; Schmieder *et al.* 2004). We explored thermal nonequilibrium in a range of flux-tube geometries characteristic of filament channels, all with steady heating localized within 1-10 Mm above the base of the corona (Antiochos, MacNeice, & Spicer 2000; Karpen *et al.* 2001, 2003, 2005, 2006).

In the present work, we determine the response of this process to a temporally varying heating rate, as predicted by many coronal heating models (see, *e.g.,* Klimchuk 2006). Assuming a uniform random distribution of pulse onset times, we examine the effects of varying the duration of the heating pulse, the average interval between heating events, and the heating deposition scale. We also investigate the influence of uniform background heating, as assumed in our earlier simulations and in models of thermal nonequilibrium in coronal loops (Müller, Hansteen, & Peter 2003; Müller *et al.* 2005; Mendoza-Briceño *et al.* 2005). We find that impulsive heating produces condensations in most cases. In contrast to the steady-heating runs, however, impulsive heating induces large flows in the system that not only delay the condensation process but also affect the location, instantaneous size, and motion of each condensation. The speed range and erratic movements of the model condensations reproduce the observed mix of counterstreaming and unidirectional flows in prominences.

2. Numerical Simulations

We performed simulations with ARGOS, our workhorse code that solves the one-dimensional hydrodynamic equations for mass, momentum, and energy with a high-order Godunov method and adaptive mesh refinement (AMR) (for further details of the basic methodology see Antiochos *et al.* 1999; Karpen *et al.* 2005). Table 1 lists the key parameters and characteristic features of the simulations performed for this study. All calculations ran for 10^5 s of simulated time after the onset of footpoint heating (see below). The same flux tube was used in all cases: the slightly dipped flux tube denoted Loop D in Karpen *et al.* (2006). The flux-tube cross-sectional area is uniform; the length is 404.77 Mm, including two 60-Mm chromospheric-photospheric sections; and the maximum height of the flux tube is 20 Mm above the chromosphere. As in our prior studies, the atmosphere is assumed to be a fully ionized plasma with a minimum temperature of 3×10^4 K. The radiative loss function is tailored to maintain the chromosphere at around 30,000 K (see Karpen *et al.* 2005, for details); below this temperature the solar radiative losses are limited by radiative transfer, which is not included in our model.

As in our earlier investigations, the heating has two components: a spatially localized component at each footpoint that is uniform in the chromosphere and falls off exponentially above with a predetermined scale λ, plus a spatially uniform background heating rate of $Q_0 = 1.5 \times 10^{-4}$ ergs cm^{-3} s^{-1} (see Karpen *et al.* 2001, for details). In all cases, an equilibrium consistent with the canonical scaling laws (Rosner, Tucker, & Vaiana 1978) was established first with only the background heating turned on. Starting at 10^5 s (t_0 =0 in the text and Figures), localized heating of the following form was imposed at each footpoint:

$$Q_e(s) = 0.1 \exp[-(s - s_0)/\lambda]/\lambda \qquad (\textit{steady heating}) \tag{1}$$

$$Q_e(s,t) = Q_e(s) * f(\delta t)\ \mathrm{sech}^{20}[(t - t_h)/\delta t] \qquad (\textit{impulsive heating}), \tag{2}$$

where Q is in units of ergs cm^{-3} s^{-1}, s is distance along the flux tube in Mm, s_0 is the position of the top of the chromosphere, $\lambda = 1$ or 5 Mm, t is the time in seconds, t_h is the array of start times for heating events, and δt is the heating pulse width (20 or 200 s). In the steady-heating runs, the footpoint heating was ramped up linearly over a 1000-s interval to avoid startup discontinuities. For the calculations with background heating turned off, the background heating was ramped down linearly in the same manner at the start of the footpoint heating.

For the impulsive heating runs, the array of interpulse intervals (onset to onset) at each footpoint was constructed as follows. A large set of uniformly distributed random numbers was generated with the Fortran 90 intrinsic functions RANDOM_SEED and RANDOM_NUMBER; a different half of this series was used for each footpoint. We then normal-

ized the range so the sum of interpulse intervals does not exceed the run length (10^5 s) and the median interval value $<$ dt $>$ is either 500 s or 2000 s (see §3.1), setting the minimum and maximum values to δt and $(2 <$ dt $> -\delta t)$, respectively. Note that heating events at a given footpoint do not overlap in time, although events at the left and right footpoints can and do overlap. The amplitude and duration of every pulse is the same for each simulation, but the amplitude is adjusted by the factor $f(\delta t)$ so the total energy input is the same for all runs and equal to that of the earlier steady-heating simulations.

3. Results

As in our earlier papers on thermal nonequilibrium, we illustrate the dynamic behavior of our model by showing the time-dependent emission intensities along the flux tube in 3 representative emission lines (see Fig. 1 caption for details): Hα proxy, O V (629 Å), and Mg X (625 Å). Side views of the flux tube emissions at selected times during three representative runs (1, 4, and 10) are shown in Figure 1, while animations 1-3, showing the continuous evolution of these runs, are available online. Figure 1 and the accompanying animations show the basic structures that develops during these runs. The steady heating runs (*e.g.,* Fig. 1a-c) all produce two condensations close in time that rapidly coalesce, forming a single central condensation that grows steadily until the end of the run. Runs with impulsive heating either form a series of transient condensations, transient condensations followed by an expanding central condensation (*e.g.,* Fig. 1d-f), or no condensation at all (*e.g.,* Fig. 1g-i).

3.1. Interpulse interval variation

We chose two test values for the average interval between heating events, $<$ dt $>$: one comparable to the coronal radiative cooling time under the assumption of constant density, and the other significantly less but greater than the longer pulse duration. The radiative cooling time is defined as:

$$\tau_r = \frac{2kT_c}{n_c \Lambda(T)} \quad , \tag{3}$$

where k is the Boltzmann constant, T_c and n_c are the coronal temperature and density, and $\Lambda(T)$ is the radiative loss function (see Fig. 1, Karpen *et al.* 2005). If the combined heating input in our model were constant and spread uniformly throughout the loop, the usual scaling laws (Rosner, Tucker, & Vaiana 1978; Vesecky *et al.* 1979) for static-loop solutions would predict $T_c \sim 3.7$ MK and $n_c \sim 9.7 \times 10^8$ cm^{-3}, yielding $\tau_r = 1960$ s. Therefore we chose

$< dt >$=2000 s and 500 s for this study.

As expected, the shorter interval yields behavior closer to the steady heating case (Fig. 2) than the longer interval. In a symmetric flux tube geometry with the same energy input at each footpoint, steady heating produces a single condensation that sits mid-loop and grows monotonically at a rate somewhat dependent on the heating scale (compare Figs. 2a and 2c).

The 500-s average interval runs all produced one or more condensations (see Figs. 3 and 4, or 8 and 9), whereas the $< dt >$=2000-s interval runs only produced condensations when the background heating was turned off (see Figs. 5 and 6, or 10 and 11). For example, Figures 3a and 5a (or 8a and 10a) directly compare runs with the same pulse width (20 s) but different $< dt >$ values. As is obvious from the lack of cool plasma in the $< dt >$=2000-s run, no condensations were formed. The role of background heating is discussed further in §3.3.

The introduction of impulsive footpoint heating greatly enhances the dynamical behavior in the flux tube over that observed with steady heating. As can be seen easily by contrasting Fig. 2 with Figs. 3-6 (also compare animation 1 with animations 2 and 3), sound waves are continually present in the impulsive-heating runs, not only varying the temperature and density but also affecting the position and size of any condensations. In some cases (*e.g.,* Run 4) this helps delay or prevent the development of a long-lived, stationary condensation as is characteristic of all symmetric steady-heating runs.

3.2. Pulse duration variation

Two pulse durations, δt = 20 s and 200 s, were used to test the effects of heating impulsiveness on the plasma behavior. The detailed evolution of these cases diverges in several significant ways, although the overall trends are similar. Because condensations always formed in the $< dt >$=500-s runs, we confine our comparison to those cases. With heating scale λ = 5 Mm, the 200-s pulses produce the first condensation nearly 2 hrs earlier than do the 20-s pulses, and the accretion rate is much higher in the 200-s case. For example, both runs with background heating turned off yield a single condensation that grows at monotonically for 26 hrs, but the growth rate is nearly 50% faster for the 200-s pulses. It is more difficult to compare the runs with background heating: both form two condensations that coalesce and fall onto the chromosphere, then form additional pairs, but the relative timing is significantly different (see Figs. 3a,c and 4a,c, or 10a,c and 11a,c).

3.3. Background heating

The presence or absence of uniform background heating greatly influences the response of long flux tubes to footpoint heating. In particular, when the average interpulse interval is comparable to the radiative cooling time, condensations form without, but not with, background heating. The strong effect of background heating is best observed by comparing Runs 10 and 11 (Figs. 5 and 10) or 13 and 14 (see Figs. 7 and 11). Without background heating, the condensations also form earlier (see Figs. 2-4), by as much as 4 hours.

In order to clarify the effects of the background heating, it is important to distinguish physically between the $<$ dt $>$=2000-s case and those with shorter interpulse intervals. For the cases with $<$ dt $>$=500-s, which is substantially less than the coronal radiative cooling time, the physics behind thermal nonequilibrium should hold, at least, in a time-averaged sense. Note that condensation formation by thermal nonequilibrium is driven by the localization of the heating, not by its time dependence. If the heating were impulsive on a 500-s time scale (on average) but spatially uniform, the flux-tube plasma would achieve a time-averaged hot equilibrium with no condensation formation. Therefore, we expect that condensations will form in the short interpulse cases as long as the localized heating dominates the uniform background heating. Consequently the ratio of the total localized heating to the uniform background heating is a critical parameter. Equations (1) and (2) imply that the energy deposited in the flux tube by the localized heating during one cycle is approximately 5 times that of the uniform heating — roughly the smallest value of the ratio for which thermal nonequilibrium still operates. Indeed, condensations do form in all of our simulations with a short interpulse interval, including the steady heating limit. In contrast, the ratio is infinite for runs with the background heating turned off, so thermal nonequilibrium is maximally effective.

The physical situation is quite different for the $<$ dt $>$=2000-s cases. Because the coronal radiative cooling time is of order 2000 s, the evolution of these flux tubes is more akin to flare-loop cooling than to thermal nonequilibrium in quasi-steady heated loops. Condensations form during flare-loop cooling through a radiative instability, in which perturbations in the initial temperature and density profiles grow faster than the loop as a whole cools (Antiochos 1980). The condensations in this case tend to be smaller and have much shorter lifetime than those for thermal nonequilibrium, which can last indefinitely and build up large mass (*e.g.,* Karpen *et al.* 2006). In fact, Figs. 5 and 6 show that, when condensations do appear in the 2000-s runs, they are small, short-lived, and infrequent. These condensations are more consistent with post-flare "loop prominences" (which are not really prominences) or coronal rain than with long-lived prominences.

The uniform background heating suppresses condensations in the $<$ dt $>$=2000-s runs

because it sets a lower limit on the density required for one to form. If this were the only heating in the flux tube, a condensation would never form; instead, the plasma would exhibit the well-known static–loop structure with a temperature maximum at the midpoint and with coronal temperature and density given by the scaling laws cited above:

$$Q_0 \sim 10^{-6} {T_c}^{7/2}/L^2 \sim n_c^2 \Lambda(T) \tag{4}$$

where L is the coronal loop half-length ($\sim$ 140 Mm), and the remaining variables are defined in §3.1. This yields the following solutions for T_c and n_c:

$$T_c \sim (10^{-6} Q_o L^2)^{2/7} \approx 2.7 \text{ MK} \tag{5}$$

$$n_c \sim \left(\frac{10^{-6} {T_c}^{7/2}}{L^2 \Lambda(T_c)} \right)^{1/2} \approx 5.3 \times 10^8 \text{ cm}^{-3}. \tag{6}$$

The initial state of the numerical model, before the localized heating is added, is in good agreement with these estimates: $T_{max} = 2.9$ MK, and $n_{min} = 5.4 \times 10^8$ cm^{-3}.

In order for a condensation to form, the density at some location in the flux tube far from the impulsive heating must remain substantially above the minimum value for a time scale of order the cooling time. This situation never occurs when $<$ dt $>$=2000 s. Instead, much of the extra material evaporated in each heating pulse drains out of the flux tube and cools down to chromospheric temperatures. For this reason, the actual cooling time for this flux tube is much longer than 2000 s, as verified by a simulation in which a single 20-s heating pulse was imposed at the same time as the background heating was turned off (not shown). The plasma temperature at the flux tube apex fell to 0.1 MK about 3 hrs after the heating pulse, because the radiative cooling time increased steadily as the coronal density decreased.

The density shortfall is evident from Fig. 12, which shows the density at a location in the flux tube leg for $<$ dt $>$=2000-s runs with and without background heating (Runs 10 and 11). For purposes of this figure only, the densities have been filtered to remove short-lived spikes due to waves and initial evaporative flows. We note that the average density in Run 11 is well below that of Run 10, which is close to the n_{min} value derived above. This density reduction also is reflected in Fig. 10, where the average baseline (excluding spikes) Mg X intensity of Run 10 clearly exceeds that of Run 11. Although condensations do form in Run 11, they form at densities far below the time-averaged density in Run 10. We conclude that the amount of long-lived extra material injected into the flux tube by the impulsive heating is simply too small to trigger condensation formation when the background heating stays on.

3.4. Heating scale

The heating scale λ was reduced by a factor of 5 in Runs 3, 6, 9, 12, and 15, without altering the total heat input per pulse or the sum over the run. Even in the steady-heating calculation (Run 3), the shorter heating scale yields higher average temperatures outside the condensation, and the condensation forms $\leq$1 hr earlier than in either run with $\lambda = 5$ Mm. With impulsive heating the λ-dependent differences become more prominent, particularly for $< \mathrm{dt} > = 500$ s (Runs 6 and 9).

For both steady and impulsive heating, the average Mg X intensity is consistently higher when $\lambda = 1$ Mm (Figs. 7c-11c) compared with $\lambda = 5$ Mm (Figs. 7a-11a), to a lesser extent when no condensations are present (*e.g.,* Runs 13 and 15). In the steady-heating cases, the minimum coronal density after the condensation has formed is approximately twice as high for Run 3 as for Run 1. With impulsive heating, the contrast in minimum coronal density is much smaller but still there; in addition, the wave-associated density spikes are significantly higher for the shorter heating scale. The intensity range is greater as well, for both O V and Mg X emissions, reflecting the stronger dynamics driven by heating pulses that are more spatially localized.

We expect more localized heating to produce higher densities, at least initially. If the heating pulse is very fast, radiative losses can be neglected and the impulsive energy deposited into the flux tube must go into creating a hot plasma. Hence

$$E_1 \sim n_1 T_1 L, \tag{7}$$

where E_1 is the total energy in a heating pulse, and n_1 and T_1 are the density and temperature of the resulting plasma. We use the maximum temperature produced by the heating pulse as an estimate for T_1. When the pulse turns on, the local coronal temperature rises rapidly until the downward heat flux balances the instantaneous energy flux due to the impulsive heating:

$$E_1/\tau \sim T_1^{7/2}/\lambda, \tag{8}$$

where τ is the pulse duration. Substituting Eq. (8) into Eq. (7) yields

$$n_1 \sim E_1^{5/7} \tau^{2/7} / (L \lambda^{2/7}) \quad . \tag{9}$$

Therefore, if we compare two heating pulses with the same total energy and duration but different deposition scales λ, the more localized pulse will produce a higher initial density. Our simulations are consistent with this relation.

3.5. Differential Emission Measure

Averaging the emission for each run over time and space essentially synthesizes the emission from a collection of flux tubes in different evolutionary states, as postulated by our prominence model. The column differential emission measure in the range log T=4.5-6.5 K was determined as follows:

$$DEM(T) = \sum_{j=1}^{N_d} \sum_{i=1}^{N_c(T)} (n_i^2 ds_i)_T \Delta T(T)/(h N_d L_{cor}) \qquad cm^{-5} K^{-1} \tag{10}$$

At 100-s intervals throughout each run, the instantaneous emission measures per cell, $n_i^2 ds_i$, were binned according to $\log_{10}$T, where each bin is 0.2 dex wide. Only cells located greater than 10 Mm above the footpoints were included, to avoid the overwhelming contribution from the flux-tube transition region. The contents of each temperature bin (total number of cells per bin = $N_c(T)$) were summed separately over the run and divided by the number of dumps, N_d, and the coronal length, L_{cor}, to obtain the averaged DEM normalized by the unknown column depth. Finally, these results were multiplied by a value of the column depth along the line of sight, h, chosen to obtain minimum DEM values comparable to those derived recently from SOHO/SUMER prominence observations (Parenti & Vial 2007).

The column depth estimated in this manner is not the same for the steady heating (Runs 1-3) and impulsive heating (Runs 4-15) runs: $h \sim 1250$ km for Runs 1-3, while $h \sim 4000$ km for the remaining runs. Much of this difference can be attributed to the symmetry of both the flux-tube geometry and the heating: the steady heating runs develop a steadily growing, static condensation, whereas impulsive heating produces shorter-lived dynamic condensations as well as single condensations that move back and forth along the flux tube as they grow. For example, consider the final state of Runs 1 and 4 (Figs. 2a and 3a): a centrally located, growing condensation exists in both cases, but occupies substantially more of the flux tube in the steady heating case (∼80 Mm) than in the impulsive heating run (∼20 Mm). To account for the observed emission intensity, therefore, the effective prominence width (i.e., column depth) would be smaller if the heating were steady rather than impulsive. SKYLAB slit-spectrograph observations of a limb prominence yielded a column depth around 1200 km at transition-region temperatures (Mariska *et al.* 1979), which is comparable to our lower estimate. The observed prominence width typically is much larger, indicating small filling factors consistent with their wispy appearance in high-resolution images. Moreover, if the steady heating symmetry were broken, our earlier studies demonstrated that a long-period cycle of dynamic condensation formation and destruction, accompanied by unsteady flows into the condensation, would occur in the same flux tube (see Karpen *et al.* 2006). In this case the estimated filling factor would be even smaller, and h would be larger, in order to match the observed DEM magnitude.

The predicted column DEMs (Figs. 13 and 14) differ from each other in several ways, the most prominent being the systematic difference in shape between the runs that formed condensations and those that did not. Figures 14b and c show this difference most clearly, because condensations only formed in Runs 11 and 14. When condensations are present in the impulsive-heating calculations, the DEM has a broad, shallow minimum above 0.1 MK and decreases precipitously above 3 MK, whereas the condensation-free DEM is measurable only at coronal temperatures above 1 MK (recall that the chromosphere and transition region at the footpoints of the flux tube have been omitted from the DEM calculations). The pulse duration has little impact on the shape or location of the minimum, although runs with δt=200 s exhibit slightly higher emission measures in general.

The steady-heating DEMs (Figs. 13a and 14a) do not resemble the impulsive-heating DEMs with or without condensations, however, nor do they agree with typical quiet-Sun or prominence DEMs (*e.g.,* Parenti & Vial 2007, Fig. 2). The steady heating DEMs have narrower, deeper mimima and are concave-downward between logT $\sim$ 5.1 and 6.3, with a peak around logT=5.9. As with the effective column depth, the predicted DEM in these cases is strongly influenced by the extreme symmetry of the simulated system, and hence is unlikely to apply to actual solar prominences.

The slope of the logDEM-logT relation is dictated by the physical processes responsible for the energy balance (see, *e.g.,* Antiochos 1980). Within the temperature range 0.1-1 MK, our simulated impulsive-heating DEMs vary approximately as $T^{0.4}$ for Runs 5 and 8 (background heating off), $T^{0.5}$ for Runs 4 and 6, $T^{0.7}$ for Runs 7, 9, and 14, and $T^{-0.9}$ for Run 11. The observed slopes range from 0.7 for Parenti & Vial (2007) to 1.5 for Cirigliano, Vial, & Rovira (2004), although the latter estimate is uncertain because no data were obtained above logT=5.7. The location of the minimum ranges from logT=5.1 for the steady heating and 2000-s runs to 5.3 for the 500-s runs. The DEMs derived from prominence observations cover a comparable range of temperatures at minimum: logT = 5.1 for Parenti & Vial (2007), 5.3 for Cirigliano, Vial, & Rovira (2004), and 5.4 for Kucera & Landi (2006). The highly dynamic nature of the features investigated by Kucera & Landi (2006) may indicate pre-eruptive activation, however, so it is not surprising that their DEMs differ from those of the quiescent prominences studied by Cirigliano, Vial, & Rovira (2004) and Parenti & Vial (2007). The quiet-prominence DEMs agree well over the temperature range in which they overlap, despite the unknown (and undoubtedly different) background contributions from the plasma surrounding the prominences.

As shown in Fig. 15, we find that the impulsive heating runs with $<$ dt $>$ = 500 s (*e.g.,* Run 4) reproduce most closely the shape, location of the minimum, and power-law temperature dependence of the observed quiet-prominence DEMs between logT=4.6 and 5.6.

At higher temperatures the curves diverge. The additional emission leading up to the peak around 1 MK in the observed DEM probably is due to the unsubtracted contribution from the background and foreground corona in the Parenti & Vial (2007) DEMs. No emission lines were observed by Parenti & Vial (2007) above logT=6.2, so the DEM at higher temperatures is unconstrained; hence we cannot compare the simulated and observed DEMs beyond this point. The impulsive-heating runs with $< \mathrm{dt} > = 2000$ s and background heating turned off (Runs 11 and 14) reproduce the overall shape and minimum location, but consistently fall below the observed DEM magnitudes, consistent with the formation of smaller condensations noted in §3.3. Increasing the column depth along the line of sight to ∼10 Mm would produce closer agreement. We conclude that heating localized around the footpoints that is impulsive but quasi-steady, with average interpulse intervals well below the radiative loss time, yields differential emission measures in close agreement with non-erupting prominence observations.

3.6. Condensation Velocity

One of the most striking differences between the steady and impulsive heating cases is in the condensation velocities. For steady heating (Runs 1-3), the condensation rapidly settles into a growing but quasi-stationary state, with small variations in the length of the condensation. Runs 1 and 2 exhibit little if any displacement of the center of mass from the flux tube midpoint, once the initial pair of condensations has coalesced. In the case with $\lambda = 1$ Mm (Run 3), however, the center of mass also oscillates around the midpoint of the flux tube from birth until the end of the calculation; the period is approximately 3 hours, while the amplitude of the oscillation grows slowly. reaching ∼3 Mm in 24 hours. With impulsive heating, both fully dynamic and quasi-stationary condensations are formed, as well as coalescing pairs (Karpen *et al.* 2006). Figure 16 shows the center of mass location vs time for Runs 4, 6, and 11. Simple linear fits to the slopes of these plots, excluding periods when the condensation reverses direction, yield speeds in the ranges 6-31 km s^{-1} (Run 4), 5-29 km s^{-1} (Run 6), and 20-115 km s^{-1}. Values for the analogous δt=200 s runs are comparable, including the increased speeds for $< \mathrm{dt} >$=2000 s with no background heating.

4. Conclusions

Our simulations demonstrate that condensations can form through thermal nonequilibrium in long, low-lying flux tubes with impulsive random heating localized above the chromosphere. For average intervals between heating pulses less than the coronal radiative cooling time, condensations form readily under the variety of circumstances tested here. For

intervals comparable to or greater than the radiative cooling time, however, condensations only form when there is no background heating in the flux tube.

One-dimensional calculations of time-dependent plasma behavior in response to impulsive heating just above the chromosphere were reported recently by Testa *et al.* (2005) and Mendoza-Briceño & Erdélyi (2006), for semi-circular flux tubes representing typical coronal loops of vastly different lengths (200 Mm and 10 Mm, respectively). These studies are not directly comparable to the prominence-oriented work discussed here, because of fundamental differences in the assumed symmetries, heating pulse characteristics, and boundary conditions. However, they also find that coronal condensations can be generated by impulsive, localized footpoint heating, with and without uniform background heating, when the pulse duty cycle is less than the radiative cooling time.

In particular, we find distinct, observable differences from the results of steady footpoint heating. The mass of each condensation is significantly greater for the steady heating case. As one might expect, impulsive heating produces a much more dynamic system, with more variations in speed and direction, ever-present waves, and some falling condensations despite the time-averaged symmetry of the energy input. The time-averaged differential emission measures also depend critically on the time variability of the heating, although in all cases the presence or absence of prominence material can be deduced from the shape of the DEM.

More observations over a wider temperature range, as could be obtained by EIS/Hinode, are needed to fully characterize the DEM of both active-region and quiescent prominences, in order to estimate the total cool mass in the majority of prominences for which only limited spectral coverage is available. The motions produced by impulsive heating vary from case to case, but in general the condensation moves back and forth in each flux tube with speeds from 5 - 30 km s^{-1}. This provides a natural explanation for the observed counterstreaming flows, without requiring significant variations in the footpoint heating rate on adjoining flux tubes as in our asymmetric steady-heating simulations (*e.g.,* Karpen *et al.* 2001).

Our extensive studies of thermal nonequilibrium have shown that a wide range of observed condensation properties can be produced by this process in flux tube geometries typical of the sheared arcade configuration, by either steady and impulsive heating just above the chromosphere. These properties include subsonic counterstreaming flows as well as stationary condensations; small knots as well as long threads; and occasional higher speed flows comparable to those derived from EUV observations (Kucera, Tovar, & De Pontieu 2003). Moreover, the close convergence between our predicted DEM curves and those derived from non-erupting prominence data strengthens the case for thermal nonequilibrium, and demonstrates the value of this common diagnostic for testing all prominence formation models. Our results place important constraints on the coronal heating properties in filament chan-

nels, if thermal nonequilibrium is indeed the process responsible for the cool, dense threads and knots comprising a prominence. To date this is the only mechanism that explains the frequent observation of cool prominence elements appearing abruptly in the corona without evidence of direct levitation or injection from below. Tests of thermal nonequilibrium in other models of prominence magnetic structure, and comparably quantitative investigations of alternative theories for the origins of prominence plasma, are urgently needed if we are to make progress in understanding solar activity.

This work has been supported in part by the NASA Solar Physics SR&T program and ONR. We thank Jim Klimchuk, Enrico Landi, Spiros Patsourakos, and the PROM team for lively and informative discussions. The referee is also thanked for improving the clarity and content of this paper.

REFERENCES

Antiochos, S. K. 1980, ApJ, 236, 270

Antiochos, S. K. & Klimchuk, J. A. 1991, ApJ, 378, 372

Antiochos, S. K., Dahlburg, R. B. & Klimchuk, J. A. 1994, ApJ, 420, L41

Antiochos, S. K., MacNeice, P. J., Spicer, D. S., & Klimchuk, J. A. 1999, ApJ, 512, 985

Antiochos, S. K., Karpen, J. T., DeLuca, E. E., Golub, L., & Hamilton, P. 2003, ApJ, 590, 547

Antiochos, S. K., MacNeice, P. J., & Spicer, D. S. 2000, ApJ, 536, 494

Anzer, U., & Heinzel, P. 2003, A&A, 404, 1139

Aschwanden, M., Schrijver, C.J., & Alexander, D. 2001, ApJ, 550, 1036

Aulanier, G., DeVore, C.R., & Antiochos, S.K. 2002, ApJ, 567, L97

Aulanier, G., and Schmieder, B. 2002, A&A386, 1106

Boris, J. P. , & Mariska, J. T. 1982, ApJ, 258, L49

Brekke, P., Kjeldseth-Moe, O., & Harrison, R. A. 1997, Sol. Phys., 175, 511

Chae, J., Denker, C., Spirock, T. J., Wang, H., & Goode, P. R. 2000, Sol. Phys., 195, 333

Chae, J. 2003, ApJ, 584, 1084

Cirigliano, D., Vial, J.-C., & Rovira, M. 2004, Sol. Phys., 223, 95

Craig, I. J. D., & McClymont, A. N. 1986, ApJ, 307, 367

Dahlburg, R. B., Antiochos, S. K., & Klimchuk, J. A. 1998, ApJ, 495, 485

Devore, C. R., & Antiochos, S. K. 2000, ApJ, 539, 954

Engvold, O. 2004, Proceedings of the IAU Vol. 2004, No IAUS223,187

Foullon, C., Verwichte, E., & Nakariakov, V. M. 2004, A&A, 427, L5

Karpen, J. T., Antiochos, S. K., Hohensee, M., Klimchuk, J. A., & MacNeice, P. J. 2001, ApJ, 553, L85

Karpen, J. T., Antiochos, S. K., Klimchuk, J. A., & MacNeice, P. J. 2003, ApJ, 593, 1187

Karpen, J. T., Antiochos, S. K., Tanner, S. E., & DeVore, C. R. 2005, ApJ, ApJ 635, 1319

Karpen, J. T., Antiochos, S. K., & Klimchuk, J. A. 2006, ApJ, 637, 531

Klimchuk J.A., 2006, Sol. Phys., 234, 41

Klimchuk, J. A., & Cargill, P. J. 2001, ApJ, 553, 440

Kucera, T. A., Tovar, M., & De Pontieu, B. 2003, Sol. Phys., 212, 81

Kucera, T. A., & Landi, E. 2006, ApJ, 645, 1525

Lin, Y., Engvold, O., & Wiik, J. E. 2003, Sol. Phys., 216, 109

Lin, Y., Engvold, O., Rouppe van der Voort, L., Wiik, J. E., & Berger, T. E. 2005, Sol. Phys., 226, 239

Mariska, J. T., & Boris, J. P. 1983, ApJ, 267, 409

Mariska, J. T., Doschek, G. A., & Feldman, U. 1979, ApJ, 232, 929

Martin, S. F., & Echols, C. R. 1994, in Solar Surface Magnetism, eds. R.J. Rutten & C. J. Schrijver (Dordrecht: Kluwer), 339

Mendoza-Briceño, C. A., Sigalotti, L. d. G., & Erdélyi, R. 2005, ApJ, 624, 1080

Mendoza-Briceño, C. A., & Erdélyi, R. 2006, ApJ, 648, 722

Mok, Y., Drake, J. F., Schnack, D. D., & Van Hoven, G. 1990, ApJ, 359, 228

Müller, D. A. N., Hansteen, V. H., & Peter, H. 2003, A&A, 411, 605

Müller, D. A. N., De Groof, A., Hansteen, V. H., & Peter, H. 2005, A&A, 436, 1067

Parenti, S., & Vial, J.-C. 2007, A&A, 469, 1109

Patsourakos, S., Klimchuk, J. A., & MacNeice, P. J. 2004, ApJ, 603, 322

Pécseli, H., & Engvold, O. 2000, Sol. Phys., 194, 73

Dynamic and Structure of Quiescent Solar Prominences, ed. E.R. Priest (Dordrecht: Kluwer)

Priest, E. R., Hood, A. W., & Anzer, U. 1989, ApJ, 344, 1010

Rosner, R., Tucker, W. H., & Vaiana, G. S. 1978, ApJ, 220, 643

Schmieder, B., Rust, D. M., Georgoulis, M. K., Démoulin, P., & Bernasconi, P. N. 2004, ApJ, 601, 530

Schrijver, C. J. 2001, Sol. Phys., 198, 325

Serio, S., Peres, G., Vaiana, G. S., Golub, L., & Rosner, R. 1981, ApJ, 243, 288

Stineman, R. W. 1980, A consistently well-behaved method of interpolation. Creative Computing, July 1980.

Testa, P., Peres, G., & Reale, F. 2005, ApJ, 622, 695

Van Ballegooijen, A. A., & Martens, P. C. H. 1990, ApJ, 361, 283

Vesecky, J. F., Antiochos, S. K., & Underwood, J. H. 1979, ApJ, 233, 987

Vourlidas, A., & Korendyke, C. 2004, AAS/SPD meeting #34, #20.09

Warren, H., Winebarger, A. R., & Mariska, J. T. 2003, ApJ, 593,1174

Zirker, J. B., Engvold, O., & Martin, S. F. 1998, Nature, 396, 440

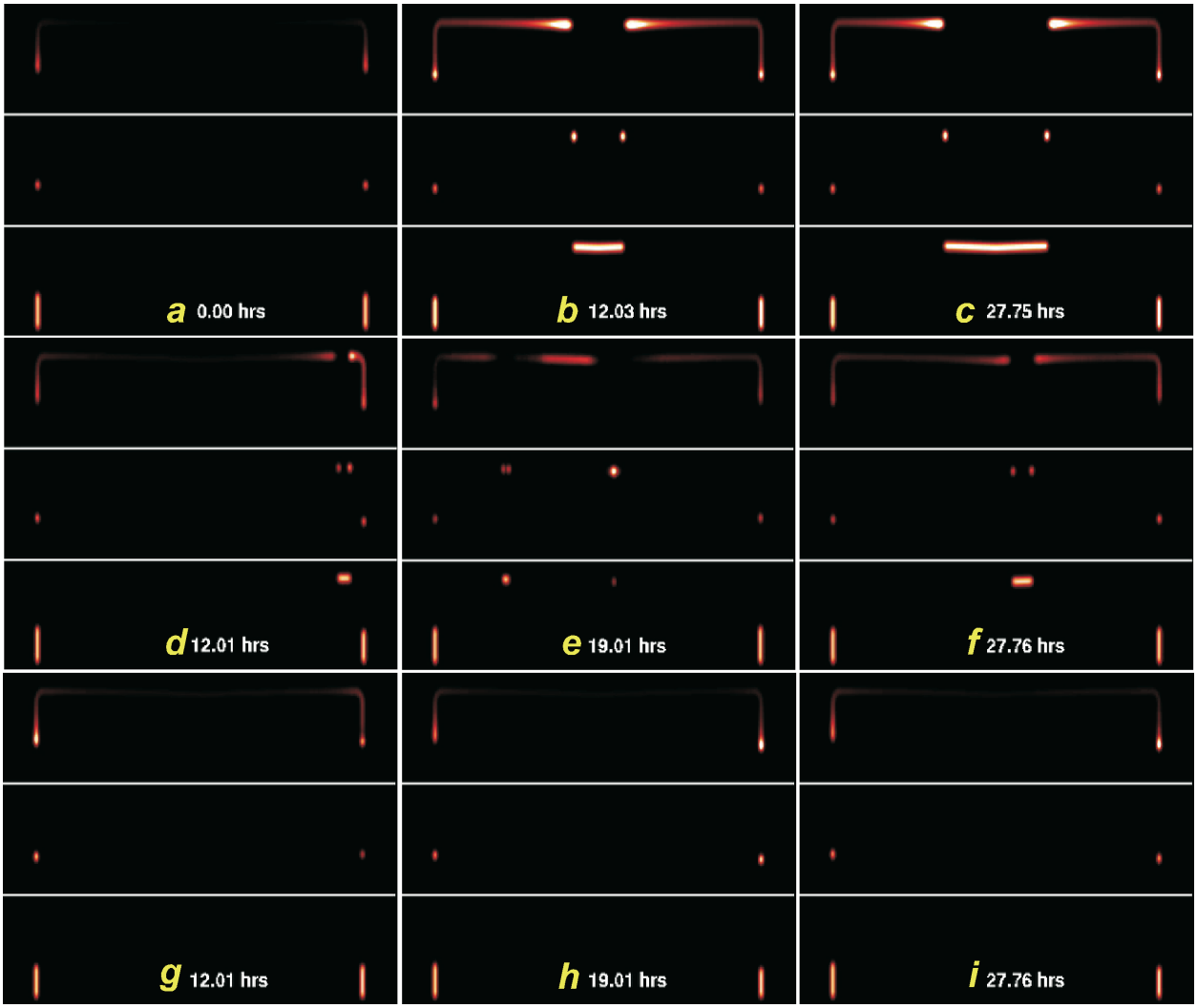

Fig. 1.— Pseudo-images of the model flux tube viewed side-on, at selected times during Runs 1 (panels *a, b, c*), 4 (*d, e, f*), and 10 (*g, h, i*). Times in hours after the onset of localized heating are shown in each panel. The righthand panel in each row shows the emissions at the end of the run. In each three-level panel, the bottom section shows the Hα proxy intensity, the middle section shows the O V (629 Å) intensity, and the top section shows the Mg X (625 Å) intensity. The Hα proxy, which is on an arbitrary intensity scale, was computed by assuming simply that all plasma at T $<$ 35000 K produces emission. The O V and Mg X intensities are computed for each grid point in an infinitely thin flux tube, modulated by the instrument response function for the SOHO CDS instrument (see our earlier papers for details). The color table is the same as shown in Fig. 2, with white (black) indicating maximum (minimum) intensity. For each ion, the intensity is normalized to the same saturation value for all runs: 5.0×10^{-5} erg cm^{-2} s^{-1} for O V (629 Å), and 1.4×10^{-6} erg cm^{-2} s^{-1} for Mg X (625 Å). This figure is also available as 3 mpeg animations in the electronic version of the ApJ.

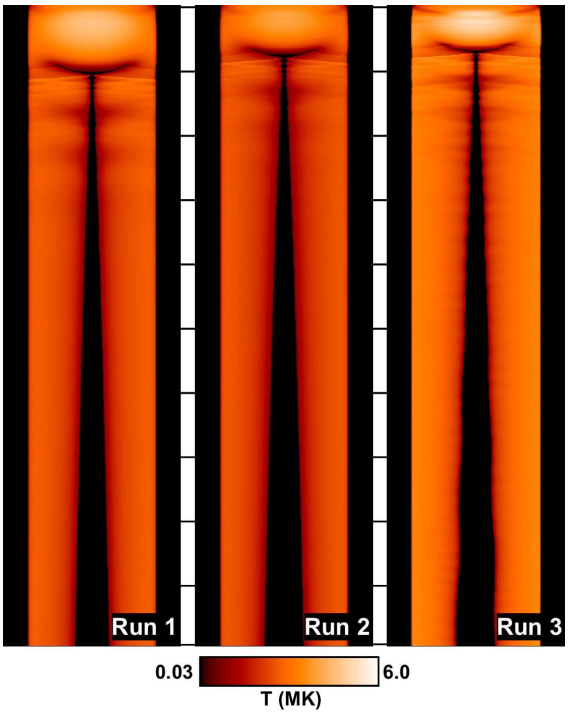

Fig. 2.— Temperature along the flux tube during Runs 1 (left), 2 (middle), and 3 (right). In each strip plot, distance along the flux tube runs from left to right, while time runs from top to bottom. The black bars between the 3 panels are spaced 10^4 s apart.

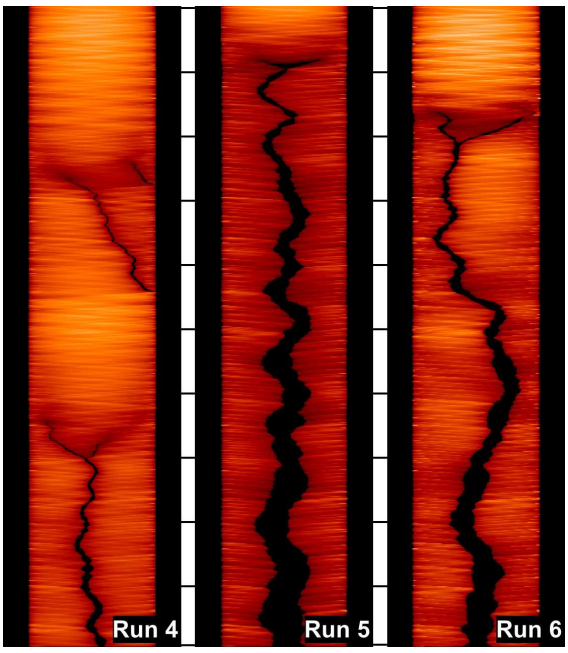

Fig. 3.— Same as Fig. 2 for Runs 4, 5, and 6 .

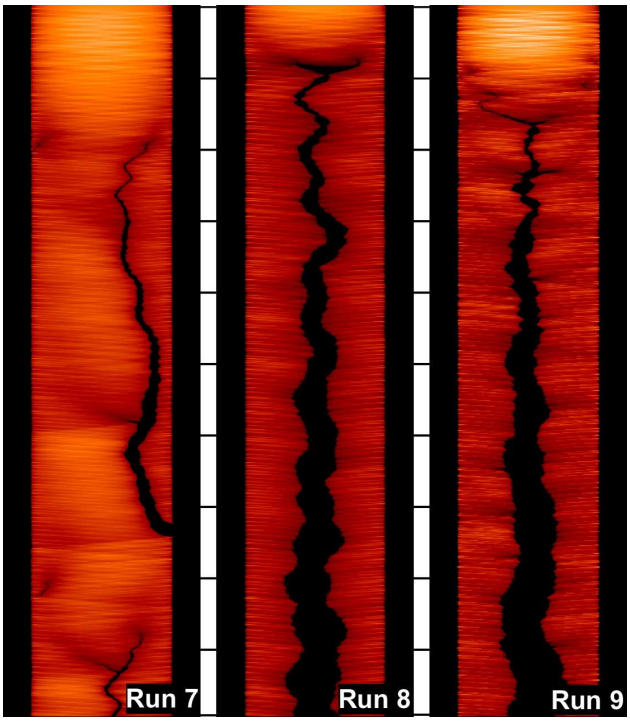

Fig. 4.— Same as Fig. 2 for Runs 7, 8, and 9.

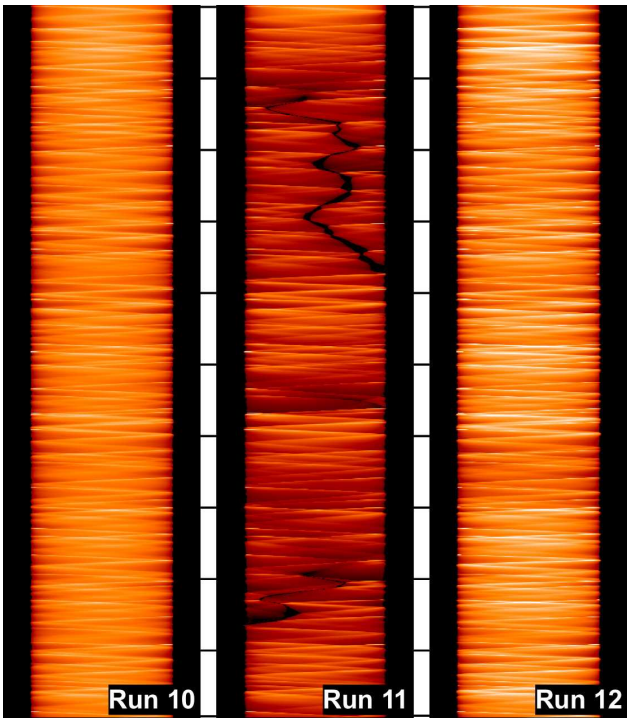

Fig. 5.— Same as Fig. 2 for Runs 10, 11, and 12.

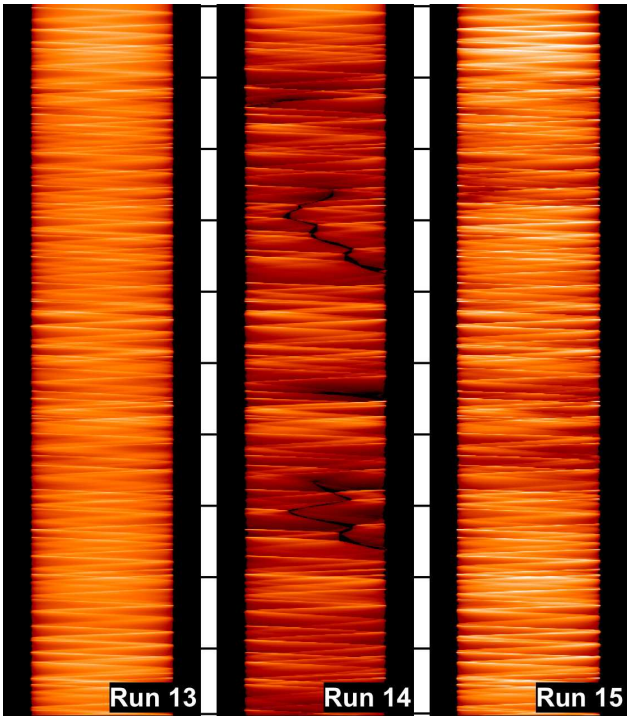

Fig. 6.— Same as Fig. 2 for Runs 13, 14, and 15.

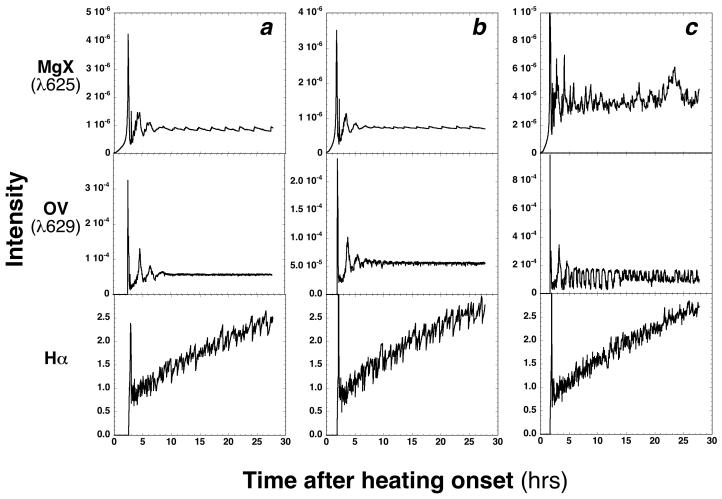

Fig. 7.— Time evolution of predicted Hα proxy *(bottom)*, O V (629 Å) *(middle)*, and Mg X (625 Å) *(top)* spatially integrated emission intensities. The instantaneous intensities were calculated as described in the caption for Fig. 1, but they were summed only over the coronal portion of the flux tube ($s = 65$ - 340 Mm) to avoid the intense stationary component around each footpoint. *(a)* Run 1. *(b)* Run 2. *(c)* Run 3.

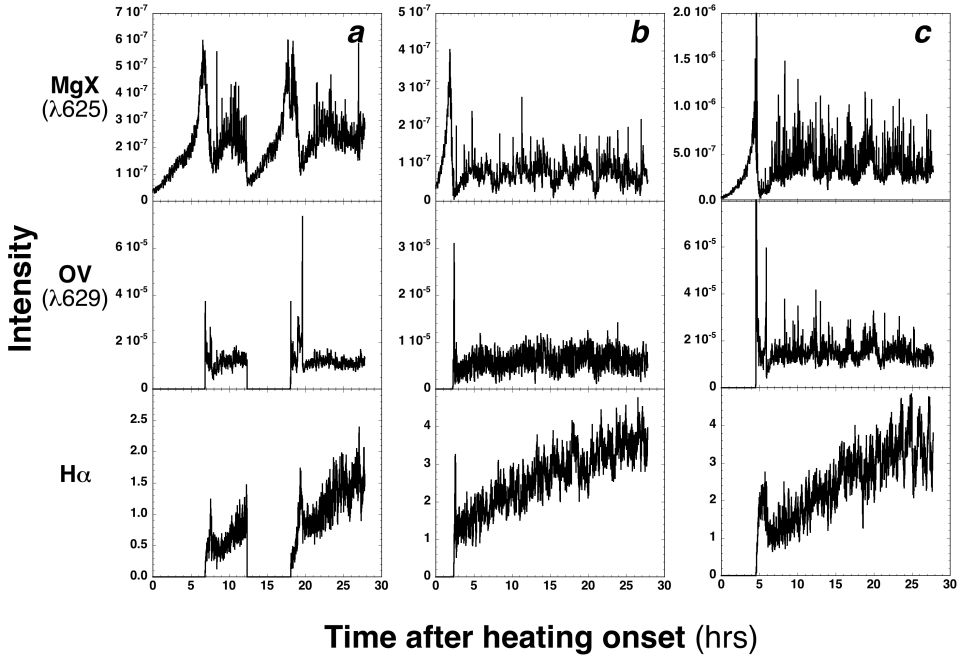

Fig. 8.— Same as Fig. 7 for Runs 4, 5, and 6.

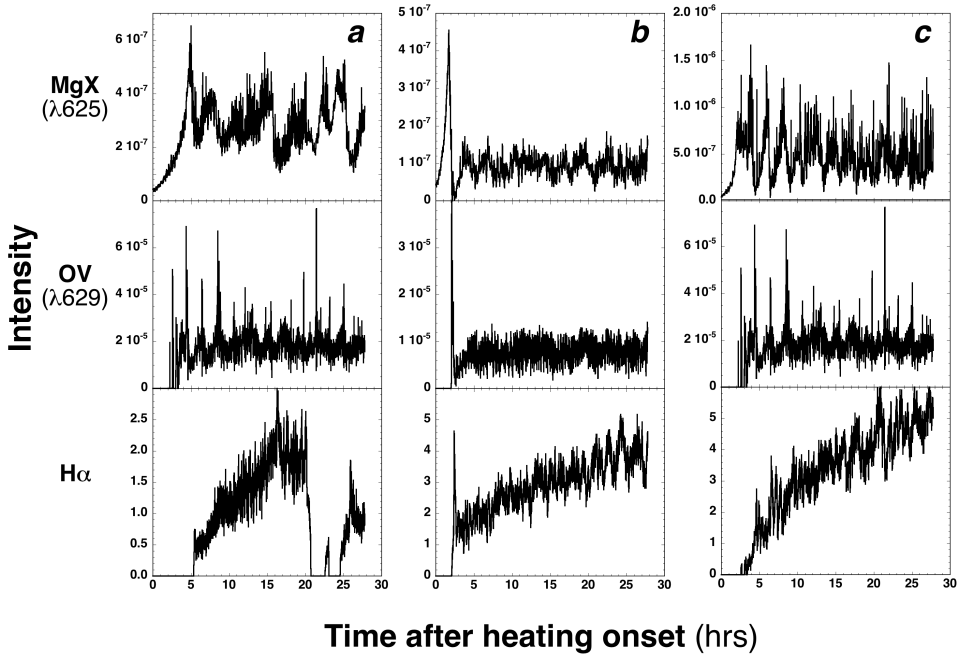

Fig. 9.— Same as Fig. 7 for Runs 7, 8, and 9.

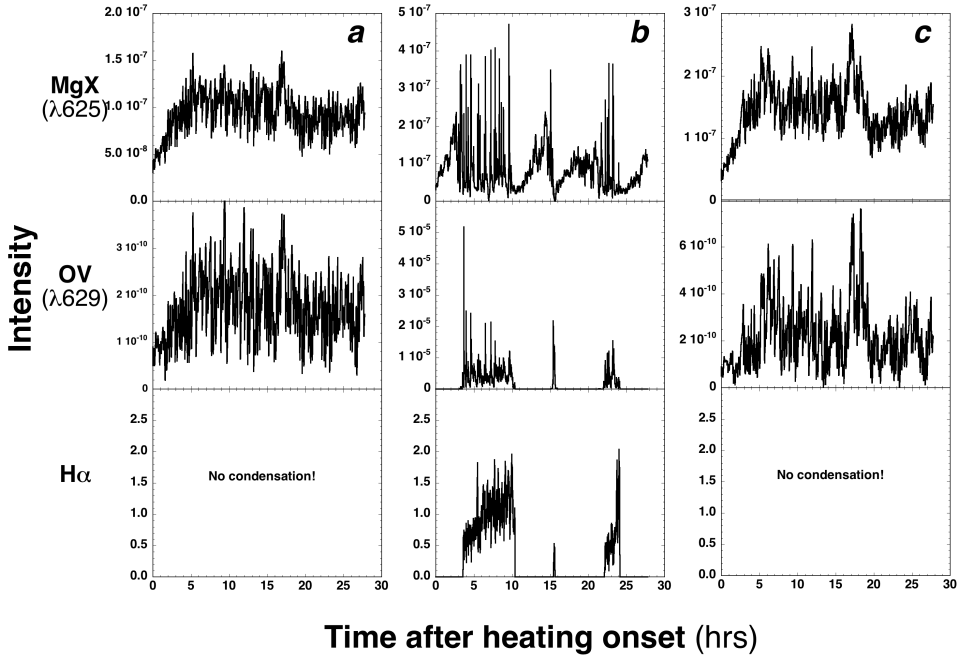

Fig. 10.— Same as Fig. 7 for Runs 10, 11, and 12.

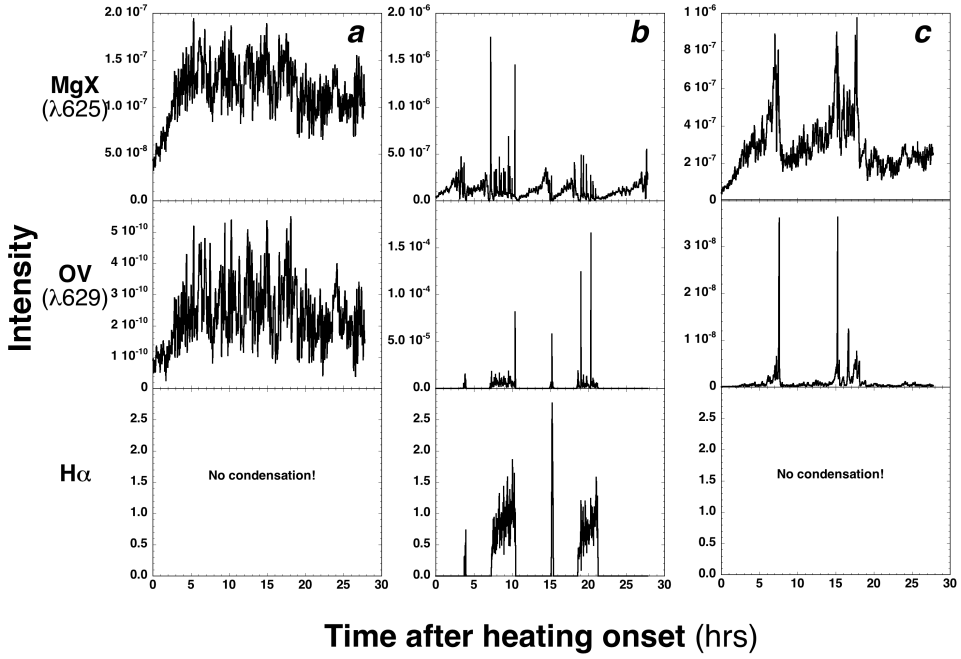

Fig. 11.— Same as Fig. 7 for Runs 13, 14, and 15.

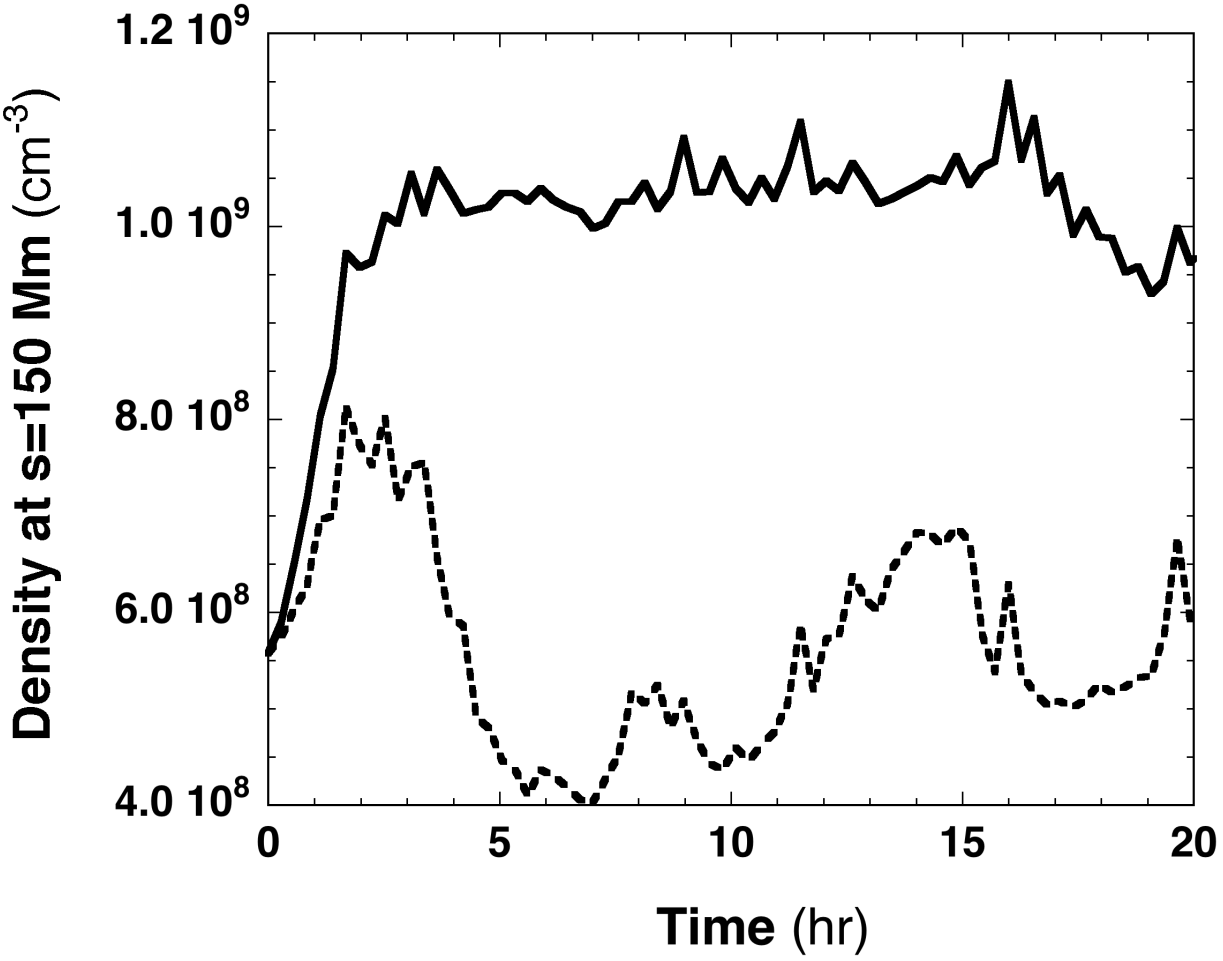

Fig. 12.— Density at $s = 150$ Mm vs. time during Runs 10 (solid line) and 11 (dashed line).

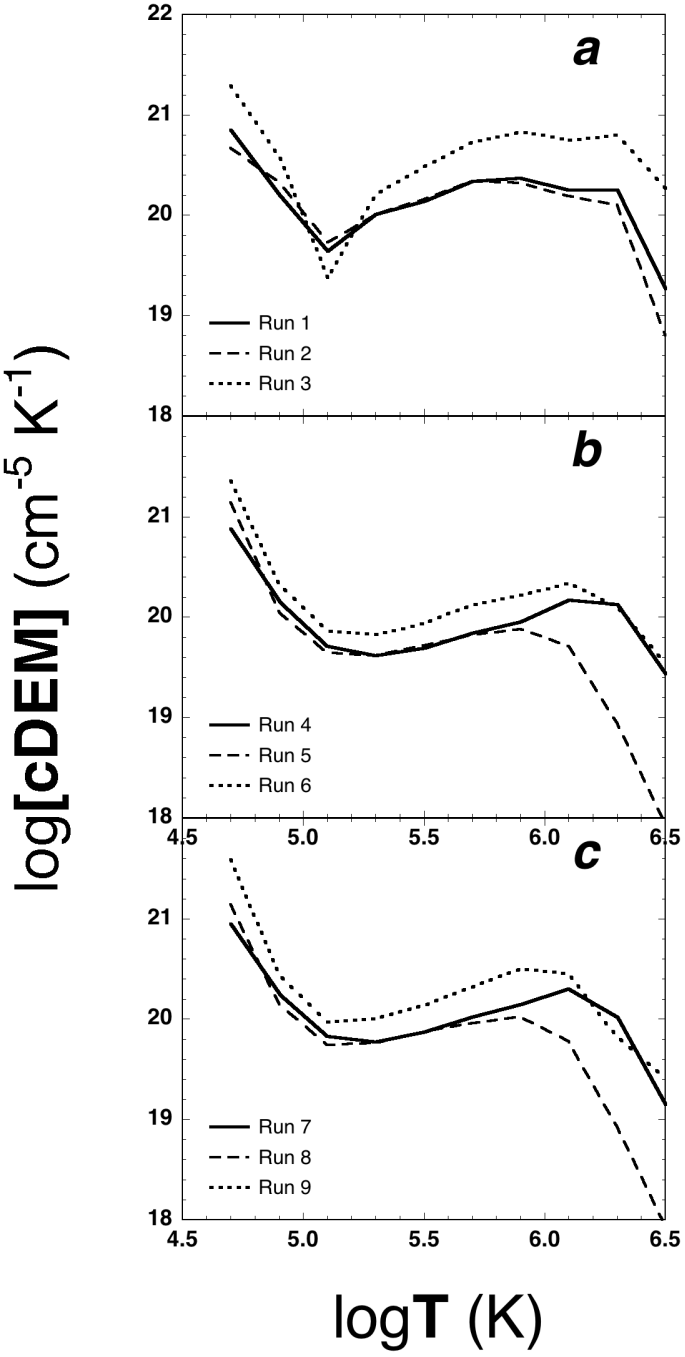

Fig. 13.— Time-averaged column differential emission measures vs. temperature. *a)* Runs 1-3. *b)* Run 4-6. *c)* Runs 7-9.

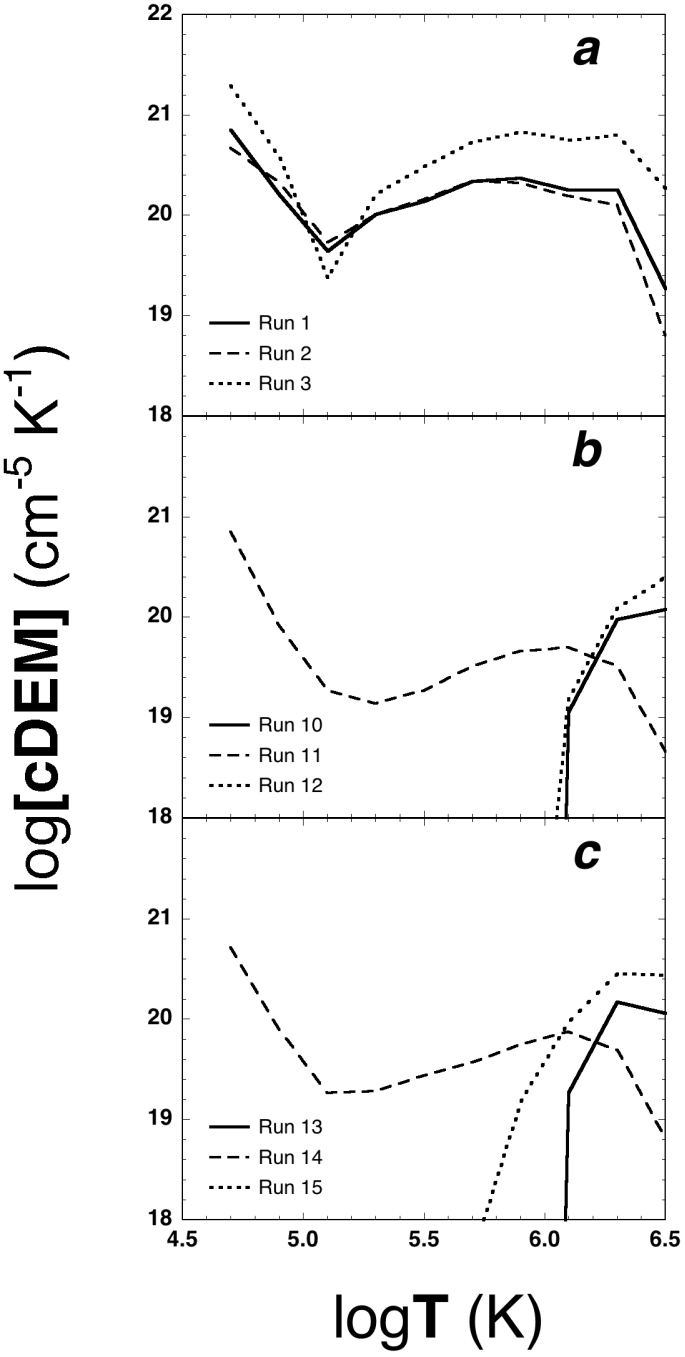

Fig. 14.— Time-averaged column differential emission measures vs. temperature. *a)* Runs 1-3. *b)* Runs 10-12. *c)* Runs 13-15.

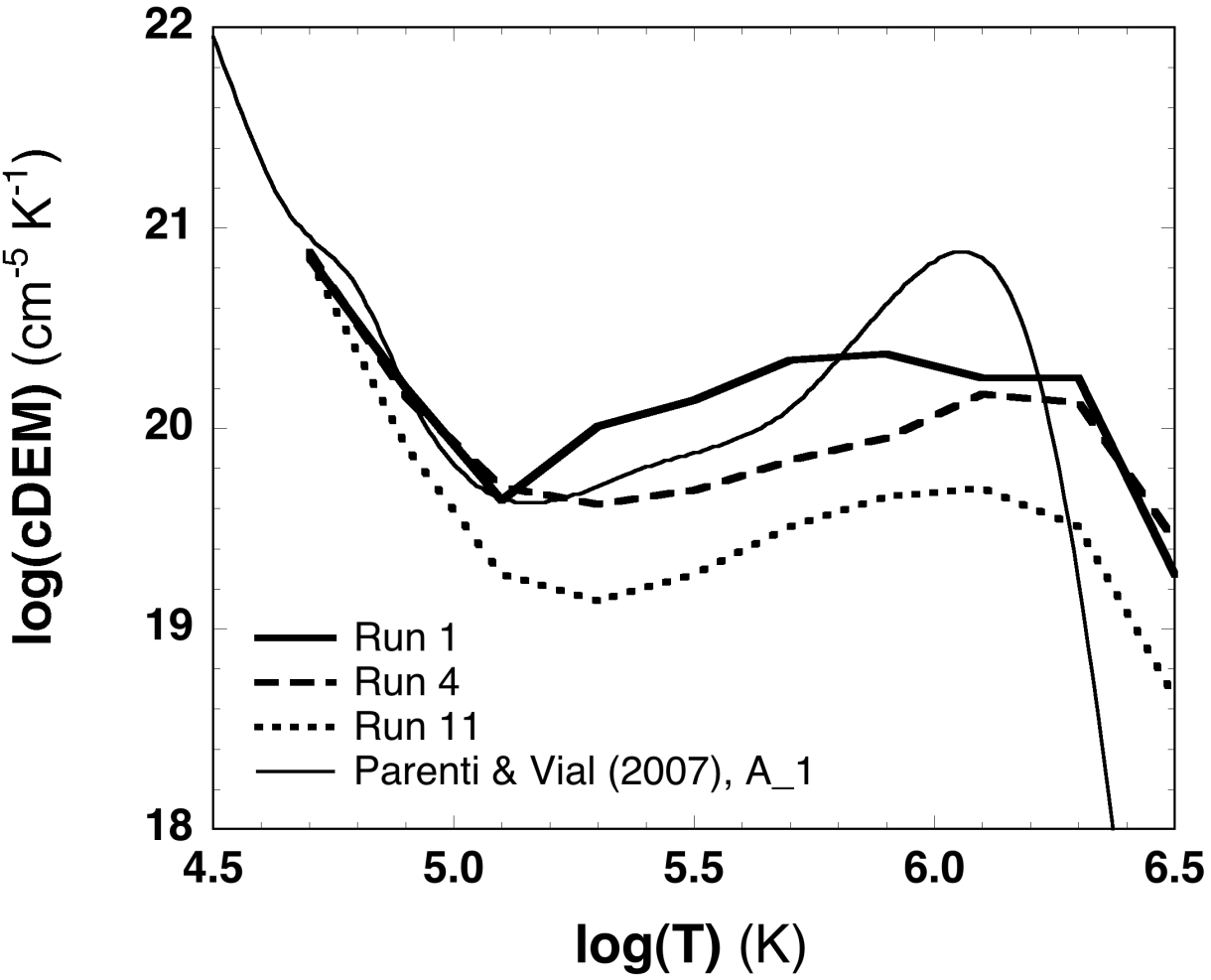

Fig. 15.— Time-averaged column differential emission measures vs. temperature for 3 condensation-forming runs (Runs 1, 4, and 11) and the best fit to the cDEM obtained by Parenti & Vial (2007) for prominence section A_1 (data courtesy of S. Parenti).

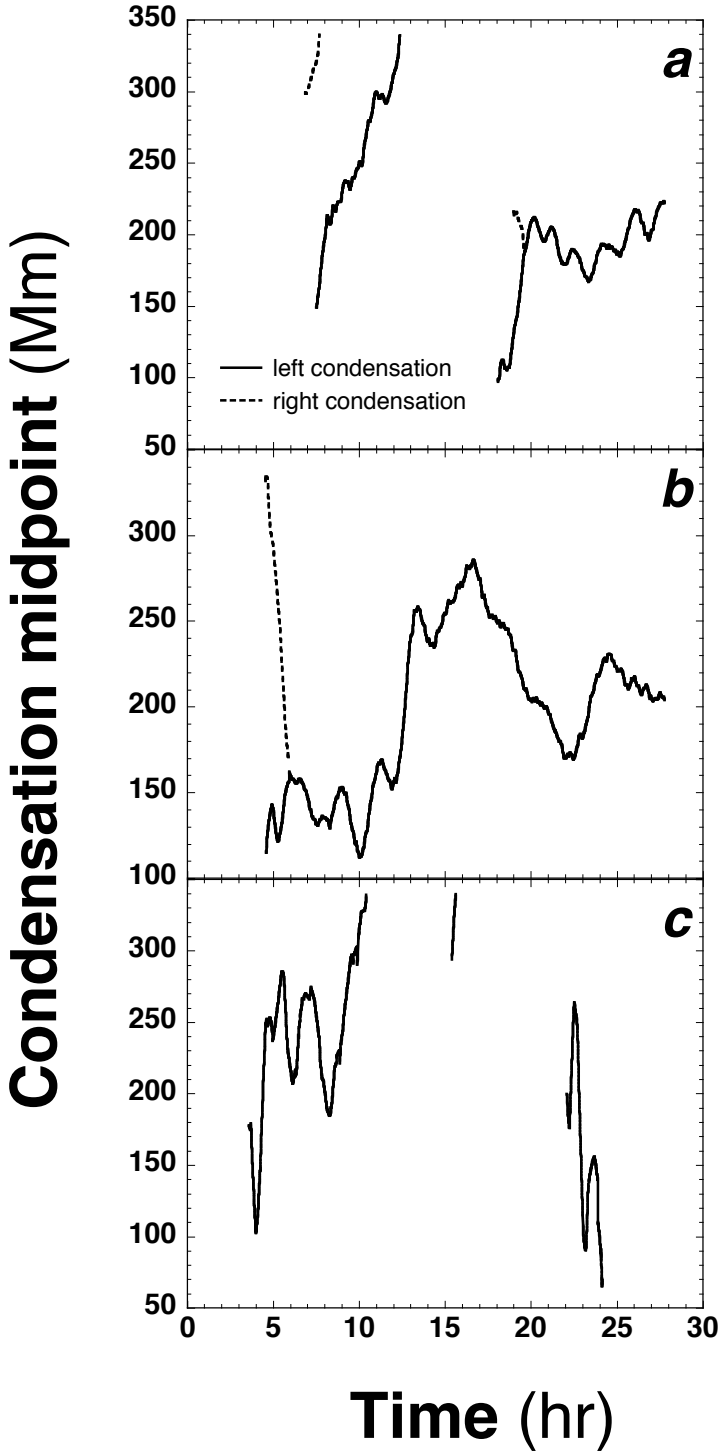

Fig. 16.— Condensation midpoint location vs. time. *a)* Run 4. *b)* Run 6. *c)* Run 11.

Table 1. Simulation Parameters

Run	Median Interpulse Interval (s)	Pulse Duration (s)	Background heating on	λ (Mm)
1	0	inf	yes	5
2	0	inf	no	5
3	0	inf	yes	1
4	500	20	yes	5
5	500	20	no	5
6	500	20	yes	1
7	500	200	yes	5
8	500	200	no	5
9	500	200	yes	1
10	2000	20	yes	5
11	2000	20	no	5
12	2000	20	yes	1
13	2000	200	yes	5
14	2000	200	no	5
15	2000	200	yes	1

Note. — See text for initial and boundary conditions common to all simulations.